Journal of Magnetism and Magnetic Materials 380 (2015) 341–346

Contents lists available at ScienceDirect

Journal of Magnetism and Magnetic Materials

journal homepage: www.elsevier.com/locate/jmmm

Same magnetic nanoparticles, different heating behavior: Influence of the arrangement and dispersive medium

Irene Andreu [a], Eva Natividad [a,*], Laura Solozábal [a], Olivier Roubeau [b]

[a] Instituto de Ciencia de Materiales de Aragón (ICMA), CSIC-Universidad de Zaragoza, Campus Río Ebro, María de Luna, 3, 50018 Zaragoza, Spain
[b] Instituto de Ciencia de Materiales de Aragón (ICMA), CSIC-Universidad de Zaragoza, Departamento de Física de la Materia Condensada, 50009 Zaragoza, Spain

ARTICLE INFO

Article history:
Received 30 June 2014
Received in revised form
23 October 2014
Accepted 25 October 2014
Available online 29 October 2014

Keywords:
Magnetic hyperthermia
Specific absorption rate
Iron oxide nanoparticles
Seeded growth synthesis
Linear response theory
Colloidal dispersions

ABSTRACT

The heating ability of the same magnetic nanoparticles (MNPs) dispersed in different media has been studied in the 170–310 K temperature range. For this purpose, the biggest non-twinned nanoparticles have been selected among a series of magnetite nanoparticles of increasing sizes synthesized *via* a seeded growth method. The sample with nanoparticles dispersed in n-tetracosane, thermally quenched from 100 °C and solid in the whole measuring range, follows the linear response theoretical behavior for non-interacting nanoparticles, and displays a remarkably large maximum specific absorption rate (SAR) value comparable to that of magnetosomes at the alternating magnetic fields used in the measurements. The other samples, with nanoparticles dispersed either in alkane solvents of sub-ambient melting temperatures or in epoxy resin, display different thermal behaviors and maximum SAR values ranging between 11 and 65% of that achieved for the sample with n-tetracosane as dispersive medium. These results highlight the importance of the MNPs environment and arrangement to maintain optimal SAR values, and may help to understand the disparity sometimes found between MNPs heating performance measured in a ferrofluid and after injection in an animal model, where MNP arrangement and environment are not the same.

1. Introduction

The heating ability of magnetic nanoparticles (MNPs) for magnetic hyperthermia [1,2] is commonly quantified by means of the specific absorption rate (SAR) [3,4], also referred to as specific loss power (SLP). This heating ability is related to the magnetization reversal processes that occur when the MNPs are subjected to an alternating magnetic field. Accordingly, SAR values depend, like magnetic properties, on temperature.

Given that magnetic hyperthermia therapy involves temperatures from 36 up to about 50 °C, it is essential to evaluate SAR in this narrow temperature range, in function of the amplitude, H_0, and frequency, f, of the applied magnetic field. Some materials may show a weak SAR variation in this range, making reasonable the use of average values for therapy planning. But in other cases, SAR values may change appreciably as temperature increases. An extreme case is found in self-regulating MNPs [5], in which the SAR drop at the temperature range of interest is the basis of their functionality.

Also, the determination of SAR in a wider temperature range may provide further information about the MNPs, needed for the feedback synthesis–characterization–application. For example, it is well-known that the thermal dependence of the out-of-phase ac magnetic susceptibility, χ'', provides useful information of certain magnetic transitions. At low H_0 values, where the linear response theory [6] is fulfilled, SAR is linearly proportional to χ'', thus providing similar information [7], but obtained with f and H_0 values more adequate for magnetic hyperthermia.

SAR(T) characterization may be also useful in the study of the behavior of MNPs in different dispersive media, where viscosity changes due to melting or pre-melting processes can allow orientation or free movement of MNPs. In this sense, the influence of the MNP colloidal environment on the temperature evolution of the magnetization, M, has been studied [8,9] under static magnetic fields, through zero-field-cooled (ZFC) and field cooled (FC) $M(T)$ measurements. Also, ac susceptibility studies have been performed on similar systems [10], using alternating magnetic fields with low amplitudes and frequencies.

In this work, we apply SAR(T) characterization to study the behavior of several systems composed of the same magnetic nanoparticles in different dispersive media and subjected to an alternating magnetic field suitable for magnetic hyperthermia. The

* Corresponding author.
E-mail address: evanat@unizar.es (E. Natividad).

http://dx.doi.org/10.1016/j.jmmm.2014.10.114
0304-8853/

different SAR(T) values and trends obtained demonstrate that, not only the intrinsic properties of the MNPs determine their heating ability, but also the spatial arrangement can enhance or reduce SAR values and shift the temperature at which the heating ability becomes maximal. Even though the experiments are not performed in physiological environment, the present findings certainly give a clue about the origin of the loss of performance of MNPs in *in-vivo* applications [11].

2. Experimental methods

2.1. Synthesis of magnetic nanoparticles

A series of magnetite nanoparticles of increasing sizes was synthesized following and adapting the original seeded growth method of Sun et al. [12,13] and a more recent study by Erné et al. to obtain so-called "facets" and "twins" nanoparticles [14]. Thus ca. 6 nm Fe_3O_4 spherical nanoparticles seeds were obtained adding $Fe(acac)_3$ (2 mmol, $>99.9\%$ trace metal basis), 1.2-hexadecanediol (10 mmol, 97%), oleic acid (6 mmol, 90%) and oleylamine (6 mmol, $>70\%$) to 20 mL benzyl ether (99%) under a flow of argon and first stirring magnetically at room temperature under Ar for 5 min. The mixture was then heated to 200 °C, maintained for 2 h at this temperature and heated to reflux (ca. 293 °C) for 1 h, under continuous stirring and flow of Ar. The rate of heating, a key parameter with respect to final nanoparticle size and shape, was the maximum attainable with our setup, at ca. 2.5 °C/min. The formed black dispersion was cooled to room temperature by removing the heat source, maintaining stirring. Once at room temperature, the reaction mixture was opened to air and ethanol (40 mL) was added, resulting in the precipitation of a black solid that was separated by centrifugation. This raw product was redispersed in n-hexane (40 mL, $>99\%$) in the presence of oleic acid (0.05 mL) and oleylamine (0.05 mL) with bath ultrasonication. After centrifugation to remove undispersed material, the product was then precipitated with ethanol (16 mL), centrifuged to remove the supernatant, and redispersed into n-hexane (16 mL) with bath ultrasonication. A first growth step was then done adding 84 mg of the obtained seeds dispersed in n-hexane to a mixture of $Fe(acac)_3$ (2 mmol), 1.2-hexadecanediol (10 mmol), oleic acid (2 mmol) and oleylamine (2 mmol) in 20 mL benzyl ether previously stirred for 5 min under a flow of Argon at room temperature. The mixture was then brought to 100 °C, temperature at which it was kept 30 min without condenser under Ar flow to evaporate the hexane. After fitting the condenser, the mixture was then warmed further and kept 1 h at 200 °C and finally refluxed 30 min, all under Ar flow. The exact same workup procedure as for the seeds was used. A total of 26 identical growth steps were then done using the exact same procedure except for the amount of nanoparticle seeds from the previous steps, now using 80 mg, and for the last seven growth steps reducing the amount of both oleic acid and oleylamine to 1 mmol. All reagents and solvents were purchased from Aldrich at the indicated purities and used without further purification.

2.2. Characterization of structure, morphology and size

The hydrodynamic size of MNPs was monitored after every five growth steps by Dynamic Light Scattering (DLS) using a Zetasizer Nano ZS from Malvern Instruments in backscatter mode using a 633 nm HeNe laser. The position of the maximum of the intensity distribution of particle sizes was used to check this size. For DLS experiments, the MNPs were suspended in hexane to reach a concentration of 0.03 mg/ml.

Complementary, given that the DLS intensity distribution does not reflect the precise size of MNPs, Transmission Electron Microscopy (TEM) images were taken after selected growth steps, in order to determine morphology and real size. Small quantities of diluted hexane ferrofluids were dropped onto carbon-coated copper grids and the solvent was left to evaporate. Observations were made on a JEOL 2000 FXII instrument working at an acceleration voltage of 200 kV.

The crystalline phase of selected nanoparticles was identified by X-ray powder diffraction (XRD). Experiments were performed with a Phillips X′per Pro diffractometer (Cu Kα radiation) on MNP powder. Diffraction patterns were recorded in the 2θ range 10–100° with a scan step of 0.03° (2θ) for 3 s.

Table 1
Summary of samples prepared for SAR(T) measurements.

Sample	*Medium*	*c (mg/g)*	*c (mg/mL)*
C6	n-Hexane	8.9	5.84
C6-bis	n-Hexane	15.3	10.10
C12	n-Dodecane	9.0	6.90
C16	n-Hexadecane	8.3	6.44
C24	n-Tetracosane	9.0	7.08
Epo	Epoxy resin	84.3	62.7

2.3. Preparation of samples for SAR(T) measurements

The MNPs obtained after the 20th growth step, selected for the study, were suspended in 4 different alkane solvents and in epoxy resin (Epofix™). A summary of the samples and their characteristics can be found in Table 1.

For the samples dispersed in n-hexane (C_6H_{14}), n-dodecane ($C_{12}H_{26}$) and n-hexadecane ($C_{16}H_{34}$), aliquots of the original ferrofluid (in n-hexane) were evaporated in weighted vials. Once the sample solid mass (MNPs + surfactant) was determined, the adequate volume of the selected organic solvent was added to reach the desired approximate concentration, and the vials were afterwards ultrasonicated in a water bath for 5 min at room temperature. Eventually, special purpose quartz containers were filled with these ferrofluids and sealed with adhesive to prevent leakages under the vacuum conditions required for the measurements.

The sample dispersed in tetracosane ($C_{24}H_{50}$) was prepared in a similar way but, due to the higher melting point of this alkane (48–54 °C), the dispersion was performed in a water bath at 100 °C under ultrasonication with a Hielscher UP200s working at 85% of its maximum power for 30 s using the S3 tip. After filling the quartz holder, the sample was thermally quenched in an ice-water bath and then sealed with the adhesive. Quenching provides a much more homogeneous final MNP distribution than slow cooling, based on visual inspection.

A last aliquot of the original ferrofluid was washed three times with diclorometane and ethanol to remove as much surfactant as possible. The solid was then dispersed in epoxy resin in a high concentration, and the mixture was heated at 60 °C for resin curing.

2.4. Determination of sample concentration

The sample concentration, c (mass of magnetic material per mass or volume of sample), was determined combining elemental analysis with measurements of first magnetization curves, $M(H)$. The Fe content was determined by Inductively Coupled Plasma-Optical Emission Spectroscopy (ICP-OES, Jobin Ybon 2000). $M(H)$ curves were measured from 0 to 5 T at 300 K in a superconducting quantum interference device MPMS-XL from Quantum Design.

An additional sample of MNPs dispersed in tetracosane was prepared in the same way as sample C24. After recording its $M(H)$ trend, this sample was digested in *aqua regia* at 90 °C and diluted

in distilled water up to a volume of 50 ml for ICP-OES analysis. Assuming stoichiometric magnetite composition of the MNPs, the specific saturation magnetization, M_S, of this sample was determined.

In addition, $M(H)$ curves of all samples collected in Table 1 were measured on the same specimen used for magnetothermal measurements. The mass of magnetic material was then calculated dividing the M_S values by the specific M_S value obtained above. Diamagnetic corrections corresponding to sample holders and solvents were determined experimentally from separate measurements and taken into account for magnetization calculations.

2.5. Measurement of heating ability

The heating ability of the MNPs was characterized through SAR (T) measurements. SAR is defined as the heating power released per unit mass of magnetic material during ac-field exposure, and can be calculated by the pulse heating method [3] as,

$$SAR = \frac{C}{m_{MNP}}\frac{\Delta T}{\Delta t} \quad (1)$$

where C (in J/K) is the heat capacity of the specimen (sample+container), m_{MNP} is the mass of magnetic nanoparticles and ΔT is the temperature increment of the specimen during an ac-field pulse of duration Δt. Accordingly, to obtain SAR(T) trends, $\Delta T(T)$ and $C(T)$ dependences must be determined.

$C(T)$ was calculated using the mass and specific heat capacity (in J/gK) of all components of the specimens at the adequate temperature range. The specific heat capacity of the quartz sample holders, epoxy resin, adhesive sealant and n-tetracosane with dispersed MNPs was determined experimentally by Differential Scanning Calorimetry (DSC) using a Q1000 device from TA Instruments and indium and sapphire as calibrants. The specific heat capacity of n-hexane, n-dodecane, n-hexadecane and magnetite were taken from the literature [15–17].

The thermal evolution of ΔT was measured using a unique special-purpose magnetothermal setup working in adiabatic conditions, and following the procedure described elsewhere [7]. In the present case, the temperature of the specimens was first decreased down to ca. 170 K. $\Delta T(T)$ values were then determined from 170 K to 315 K on heating ramps achieved by applying successive ac-field pulses of duration Δt. During each pulse, the specimen releases heat and undergoes self-heating. ΔT is then calculated as T_2-T_1, where T_2 and T_1 are, respectively, the backward and forward extrapolation of the temperature drifts after and before the ac-field application, at the midpoint of Δt. Each ΔT value is divided by Δt and assigned to the midpoint temperature $T=(T_1+T_2)/2$. Finally $\Delta T(T)$ is used together with $C(T)$ and m_{MNP} to calculate SAR(T), according to Eq.(1). Measurements were performed with ac-field frequency and amplitude of 111 kHz and 3 kA/m, respectively, in order not to overtake the traditional biological range of ac-field application in humans [18] and study the low-field heating of the nanoparticles.

3. Results and discussion

3.1. Series of magnetic nanoparticles

Confirmation of the iron oxide phase expected to form under the used synthetic conditions, *i.e.* magnetite, [12,13] was obtained from XRD. Fig. 1 shows the typical XRD pattern of the powder, in this case obtained after the 19th growth step, showing that the crystalline structure of the MNPs is essentially magnetite.

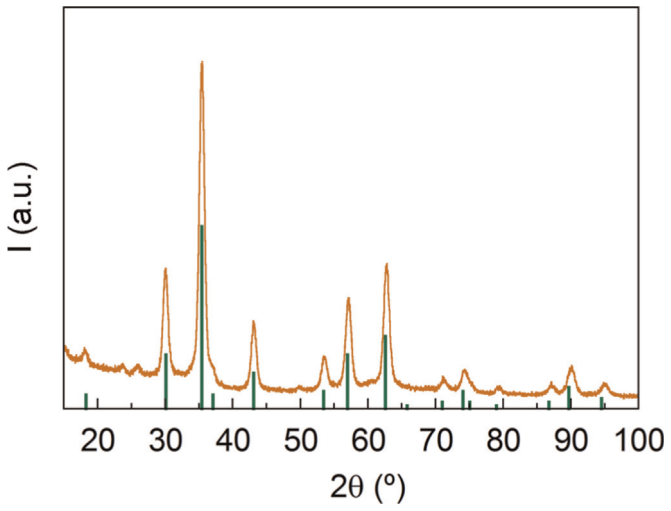

Fig. 1. XRD patterns of MNP powder (continuous line) compared with the Fe_3O_4 peak positions from database reference (bars).

The hydrodynamic size of MNPs derived from first order DLS experiments, although a few nanometers bigger than the real MNP size, is a good guiding parameter of the growth process, provided that MNPs are narrow-sized and non-agglomerated, which was the case here. Fig. 2 displays this size, measured after every five growth steps, corresponding to the position of the maximum of the intensity distribution obtained with DLS.

According to Fig. 2, the hydrodynamic size of the seeds is 9.8 nm. At the 5th growth step, this size is already 17.5 nm, and scarcely increases during the following steps in which 2 mmol of oleic acid and oleylamine are used in the synthesis. This is actually very similar to the trend observed by Luigjes et al. through TEM for their "twins" series [14]. From the 21st growth step, the amount of both oleic acid and oleylamine was reduced to 1 mmol, with the aim of allowing further growth of the MNPs, and reaching a size of about 20 nm. This growth is indeed observed in the hydrodynamic sizes of 25th and 27th growth steps. However, the width (not shown) of the DLS intensity distribution also increases, indicating higher polydispersity.

TEM images of selected growth steps shown in Fig. 2 reveal that MNPs between the 5th and the 20th growth step are not spherical but polyhedral, with rather similar shapes and a narrow size distribution. However, MNPs of the 27th growth step display more dissimilar shapes, and a wider size distribution, confirming the DLS observations. A closer inspection indicates the MNPs of these

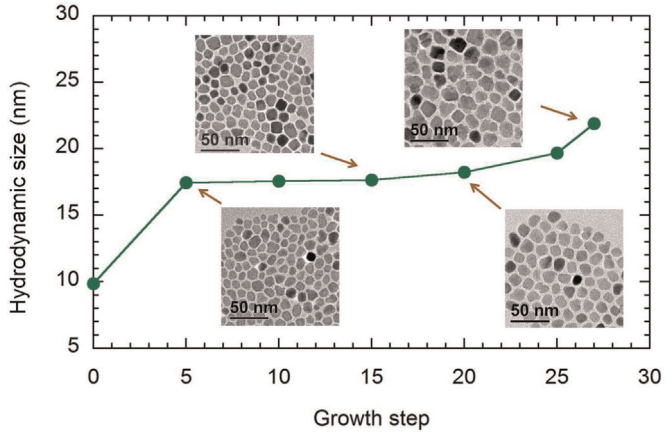

Fig. 2. Hydrodynamic size corresponding to the position of the maximum of the intensity distribution obtained with DLS, together with TEM images of selected growth steps.

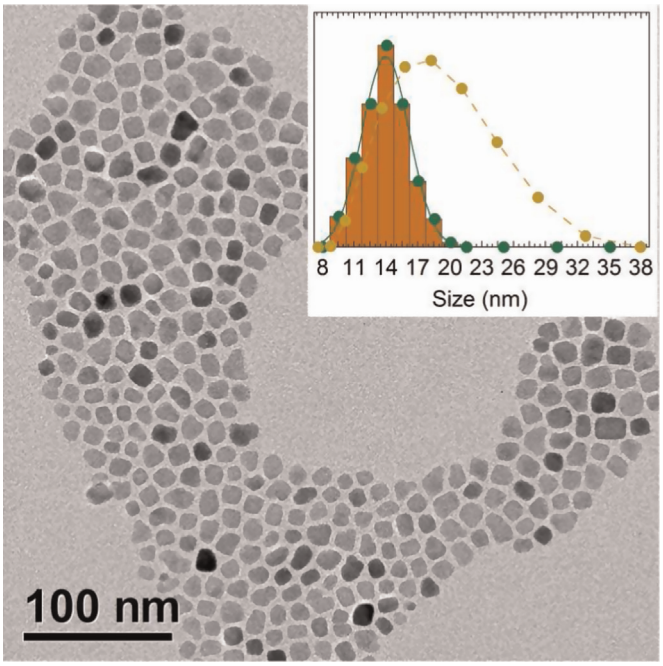

Fig. 3. TEM image of MNPs of the 20th growth step, together with the TEM size histogram fitted to a normal distribution (circles with continuous line) and the DLS intensity distribution (circles with dashed line serving as guideline).

last growth steps are essentially twinned or multiple-domain particles, again in qualitative agreement with previous work [14]. It is interesting to note that the comparatively slower rate of heating used here has only little influence on the *relative* growth of MNPs size or on the growth mechanism resulting in the formation of "twins", and only results in smaller MNPs.

Considering the above results, MNPs of the 20th growth step were selected for the magnetothermal study. Although smaller than initially pursued, they are more homogeneous in size and shape than bigger MNPs obtained by reducing the amount of surfactant. More importantly, no significant twinning effects of the particles are detected. Although of larger size, these twinned particles were shown to have a significantly smaller size of the magnetic domains than that of the whole particle [14], which could be detrimental for the heating efficiency. Fig. 3 displays a bigger TEM image of the selected sample, together with the size histogram, obtained by measuring the diagonal of 300 MNPs from several TEM images, and the DLS intensity distribution. According to TEM, the selected particles present a normal size distribution, with a mean value of 13.9 nm and a standard deviation of 2.2 nm. DLS intensity distribution indicates that the sample does not present aggregates in hexane at low concentrations.

3.2. Samples for SAR(T) measurements

Six samples were prepared for SAR(T) characterization, using MNPs coming from the same synthetic batch obtained after the 20th growth step. The specific saturation magnetization of this batch, evaluated through a sample dispersed in n-tetracosane, is M_S=81.26 emu/g, only slightly lower than that of bulk magnetite, (86.1 emu/g), in accordance with the crystalline phase obtained by XRD.

According to Table 1, samples C12, C16 and C24 have similar concentrations, ranging between 6.44 and 7.08 mg/mL. Samples C6 and C6-bis show, respectively, slightly lower and higher concentrations than the other alkane samples. All these samples display MNPs well dispersed in their dispersive media. MNPs in Epo, however, presents a strongly inhomogeneous distribution. This implies that, even if the average concentration of this sample is 62.7 mg/mL, the local concentration of MNPs is undoubtedly much higher. In addition, the surfactant of these MNPs was eliminated to facilitate their dispersion in epoxy resin, surely allowing very small interparticle distances in certain areas.

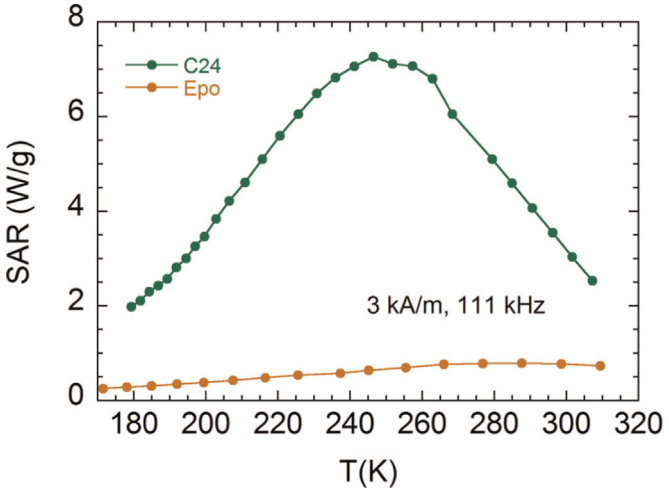

Fig. 4. SAR(T) trends of samples C24 and Epo, solid in the whole T range.

3.3. SAR(T) results for solid samples

Fig. 4 displays the SAR(T) trends of samples C24 and Epo, which are solid in the whole measurement temperature interval. In addition, Table 2 collects, among others, some key parameters of these results.

Sample C24, thermally quenched from the liquid state, is expected to preserve a well-dispersed MNP distribution. Its SAR(T) trend presents a maximum of 7.3 W/g at 246 K. This value is remarkably high, taken into consideration the used set of ac-field parameters. Indeed a recent discussion on SAR values and extrapolations [19] shows that the SAR of magnetosomes [20], one of the highest found in literature, changes from 960 W/g, at 410 kHz and 10 kA/m, to 12.8 W/g under the conditions used in this work (111 kHz and 3 kA/m), a value of the same order as the maximum SAR achieved by sample C24.

As explained in the introduction, SAR(T) is linearly proportional to $\chi''(T)$ when the linear response theory (LRT) is fulfilled. In these conditions, the relationship between both magnitudes is

$$SAR = \frac{\pi\mu_0}{\rho} f H_0^2 \chi'' \tag{2}$$

where μ_0 is the permeability of free space and ρ is the mass density of the magnetic material. According to Carrey et al. [6], in

Table 2
Summary of SAR(T) results.

Sample	$T_{melting}$ (K)[a]	SAR_{max} (W/g)	T_{SARmax} (K)
C6	173–181	4.6	229
C6-bis	173–181	4.8	222
C12	260–270	2.7	273
C16	279–295	3.0	271
C24	> 320	7.3	246
Epo	–	0.8	288

[a] Melting temperature intervals were extracted from heat capacity measurements in Refs. [16] and [15].

non-interacting MNP systems, LRT is valid when

$$H_0 < \frac{k_B T}{\mu_0 M_S V_M} \tag{3}$$

where k_B is the Boltzmann constant, and V_M is the magnetic volume of each MNP. Assuming cubic MNPs to calculate V_M, using the size determined by TEM and a mass density of magnetite of 5.2 g/cm^3 to convert the measured M_S to SI units, the maximum H_0 value allowed by Eq. (3) at the lowest considered temperature (170 K) is 4.5 kA/m, neglecting the thermal dependence of M_S.

Since measurements were carried out at 3 kA/m, the LRT is fulfilled in the T measuring interval. This implies that SAR(T) can be used to locate the onset of the superparamagnetic behavior of the studied MNPs by means of the blocking temperature, T_b, temperature at which $\chi''(T)$ and, consequently, SAR(T), are maximum. Given that sample C24 is solid in the whole measurement interval, the maximum observed can only be assigned to the unblocking of Néel relaxation mechanism, whose characteristic time, τ_N, is defined as

$$\tau_N = \tau_0 \exp\left(\frac{KV_M}{k_B T}\right) \tag{4}$$

where τ_0 is a constant, usually taken as 10^{-9} s, and K is the anisotropy constant of the MNPs. Knowing that at T_b, $2\pi \cdot f \cdot \tau_N = 1$ [21], τ_N and K can be estimated using our data. A K value of 26 kJ/m^3 is obtained, in the range of that of bulk magnetite, 23–41 kJ/m^3 [21].

This analysis leads to interpret that sample C24 is scarcely affected by interparticle interactions, and that 246 K is the blocking temperature of the Néel relaxation mechanism of its non-interacting MNPs. Bigger MNPs would have displayed T_b values nearer to room temperature, being more adequate for magnetic hyperthermia applications. Equally, the use of higher ac-field frequencies would have shifted this maximum to higher temperatures.

The maximum theoretical SAR value acquired by this sample can be calculated using Eq. 2 and the expressions for χ'' and χ_0 in reference [21], namely,

$$\chi'' = \chi_0 \frac{2\pi f\tau}{1 + (2\pi f\tau)^2} \quad \text{and} \quad \chi_0 \cong \chi_i = \frac{\mu_0 M_S^2 V_M}{3k_B T} \tag{5}$$

where χ_0 can be approximated to the initial susceptibility of the sample. Note that, at T_b, $\chi'' = \chi_0/2$. The calculated and experimental values for sample C24 are 7.9 W/g and 7.3 W/g, respectively, again neglecting the thermal dependence of M_S. This result reveals a really good *quantitative* agreement between experimental and analytical results in *SAR* measurements of MNP systems, scarcely found in the literature.

Contrary to the high SAR values of C24, sample Epo shows a dramatically lower heating performance, consequence of the high agglomeration state of its MNPs. Indeed, their maximum SAR is just 11% of that of sample C24. This result illustrates the disparity sometimes found between MNPs performance in a well-dispersed ferrofluid and after injection in an animal model, where MNPs agglomerate by cellular uptake and adhesion to tissue [22]. Other feature of the highly interacting state of this sample is the shift of its blocking temperature 42 K to higher temperature [23].

3.4. SAR(T) results for liquid samples

Fig. 5 shows the SAR(T) evolution of samples C6, C6-bis, C12 and C16 which are all liquid at room temperature, but not in the whole measurement interval. Table 2 collects key parameters of these results.

The first outstanding result is that none of these SAR(T) trends achieve the maximum SAR value of 7.3 W/g displayed by the solid sample C24, even if samples C12 and C16 are also solid at the blocking temperature of C24, 246 K. Another remarkable result is

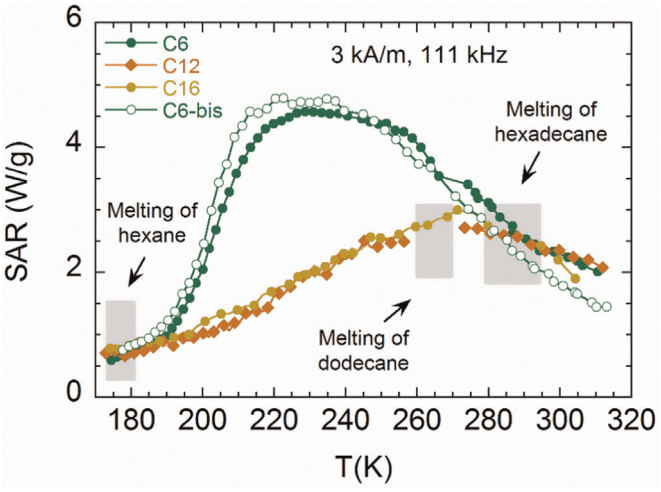

Fig. 5. SAR(T) trends of samples C6, C6-bis, C12 and C16, liquid at room T. Grey zones delimit the melting intervals of organic solvents according to heat capacity measurements in Refs. [15] and [16].

that all trends start together and converge (except that of C6-bis) at high temperatures.

Samples C6 and C6-bis, the least and most concentrated liquid samples, respectively, display very similar SAR(T) trends. This fact indicates that the slight concentration differences between these samples are not a significant parameter to be taken into account at studying their heating behavior. The maximum SAR of these samples is about 65% that of sample C24, and is achieved at lower temperatures (229 and 222 K), when the samples are in liquid state. In fact, these samples are liquid in the whole temperature range since, although they are about to solidify at 170 K, the typical solidification thermogram is not observed in the cooling trends previous to measurements. Samples C12 and C16 do solidify during cooling down to 170 K. Their SAR(T) show a similar and continuous increasing trend up to the melting temperature, after which a continuous decrease takes place. Maximum SAR values are achieved at the trend-change temperatures, and are about 40% that of sample C24.

At this point, it must be recalled that SAR(T) measurements take place under zero static magnetic field. The cooling process takes place without any magnetic field and the measuring heating ramp is achieved by the self-heating of the sample subjected to successive alternating magnetic field pulses. Therefore, the observed behaviors cannot be related to texturing or arrangements induced by the application of a dc magnetic field.

One possible explanation for the different behaviors of the liquid samples is that, due to the slow cooling rate of these samples, MNPs may gradually acquire a certain spatial arrangement upon solidification. This cannot occur in sample C24, thermally quenched. For example, ac susceptibility studies on similar ferrofluids [10] reveal that solvent freezing significantly affects the interparticle dipole-dipole interaction, causing characteristic spin-glass-like dynamics. In our case, further characterization is needed to make such a statement.

Given that the SAR data of samples C6, C6-bis, C12 and C16 is similar between 170 and 190 K, the acquired arrangement is expected to be also similar. From 190 K, samples C6 and C6-bis readily lose this arrangement, but still their SAR(T) trends do not join that of C24. This suggests that the transition between the formed arrangement and the well-dispersed state is not fully accomplished, maybe due to the successive application of ac-field pulses. The continuous increase of SAR(T) for samples C12 and C16 in the solid state, up to solvent melting temperature, suggests that the blocking temperature of the formed arrangement lies beyond their melting temperatures. Eventually, once all samples are liquid,

they display similar SAR(T) trends, which allows to discard the presence of an appreciable contribution of Brown relaxation mechanism to SAR. Indeed, since the viscosity of the solvents at 298 K are appreciably different, at 0.300, 1.383, and 3.032 mPa·s for samples C6, C12 and C16 respectively, a predominance of Brown relaxation would result in SAR differences, not observed. Also, it has to be noted that the presence of MNPs is expected to induce changes in the viscosity of the solvent, even more noticeable under the presence of a magnetic field [24]. This effect makes difficult the estimation of the Brownian characteristic relaxation times.

A final remark about the observed behaviors is that no sharp SAR increases due to possible pre-melting processes have been observed before the melting intervals. Incoherent melting at the solvent-MNP interfaces has been shown to allow physical reorientation of spatially fixed MNPs, leading to sharp magnetization increases in presence of static or dynamic magnetic fields [9,10,19], as well as to SAR increases in presence of alternating magnetic fields [19]. In the present case, the similarity between the SAR(T) trends of samples C12 and C16, with different melting and possibly pre-melting temperatures, leads to discard such effect.

4. Conclusion

A series of magnetite nanoparticles of increasing sizes have been synthesized following and adapting existing methods in the literature. Remarkably, the slower heating rates used in the synthesis due to setup restrictions result in smaller MNPs, but has only little influence on their relative growth or on the formation of twinned particles.

The biggest non-twinned MNPs have been selected for SAR(T) measurements, dispersed in several liquid or solid dispersive media, in order to explore the thermal dependence of their heating behavior in different arrangements and environments. One important result is the achievement of a non-interacting MNP distribution in thermally quenched n-tetracosane. This assembly displays a blocking temperature and a maximum SAR value in very good quantitative agreement to the linear response theory for non-interacting MNPs. In addition, this maximum SAR value is comparable with that of magnetosomes at similar amplitude (3 kA/m) and frequency (111 kHz) of the alternating magnetic field.

None of the samples dispersed in solvents that are liquid at room temperature reaches the maximum SAR value of the sample dispersed in n-tetracosane. This is possibly due to the formation of certain structures with higher blocking temperatures during the slow cooling of these samples previous to solidification. Eventually, MNPs without surfactant and non-homogeneously dispersed in epoxy resin exhibit only an 11% of the heating ability of the non-interacting sample dispersed in n-tetracosane.

As final remark based on the above results, the same MNPs may present many different heating behaviors depending on their arrangement and environment. Accordingly, MNP spatial distribution should be better characterized *in-vitro* and better controlled *in-vivo* in order to reach good correlations between the heating abilities measured in the laboratory and those achieved in magnetic hyperthermia treatments.

Acknowledgment

This work has been funded by the Spanish MINECO and FEDER, projects, Grants no. MAT2007-61621 and MAT2011-24284, and by the University of Zaragoza and Banco Santander Central Hispano S.A., Project UZ2012-CIE-10. I. Andreu thanks the Spanish CSIC for her JAE-Predoc contract. The use of Servicio General de Apoyo a la Investigación-SAI, Universidad de Zaragoza is also acknowledged.

References

[1] A. Jordan, R. Scholz, P. Wust, H. Fähling, F. Roland, Magnetic fluid hyperthermia (MFH): cancer treatment with AC magnetic field induced excitation of biocompatible superparamagnetic nanoparticles, J. Magn. Magn. Mater. 201 (1999) 413–419.
[2] B. Kozissnik, A.C. Bohorquez, J. Dobson, C. Rinaldi, Magnetic fluid hyperthermia: Advances, challenges, and opportunity, Int. J. Hyperth. 29 (2013) 706–714.
[3] I. Andreu, E. Natividad, Accuracy of available methods for quantifying the heat power generation of nanoparticles for magnetic hyperthermia, Int. J. Hyperth. 29 (2013) 739–751.
[4] S. Huang, S.Y. Wang, A. Gupta, D.A. Borca-Tasciuc, S.J. Salon, On the measurement technique for specific absorption rate of nanoparticles in an alternating electromagnetic field, Meas. Sci. Technol. 23 (2012) 035701.
[5] E. Natividad, M. Castro, G. Goglio, I. Andreu, R. Epherre, E. Duguet, A. Mediano, New insights into the heating mechanisms and self-regulating abilities of manganite perovskite nanoparticles suitable for magnetic fluid hyperthermia, Nanoscale 4 (2012) 3954–3962.
[6] J. Carrey, B. Mehdaoui, M. Respaud, Simple models for dynamic hysteresis loop calculations of magnetic single-domain nanoparticles: application to magnetic hyperthermia optimization, J. Appl. Phys. 109 (2011) 083921.
[7] E. Natividad, M. Castro, A. Mediano, Adiabatic magnetothermia makes possible the study of the temperature dependence of the heat dissipated by magnetic nanoparticles under alternating magnetic fields, Appl. Phys. Lett. 98 (2011) 243119.
[8] G. Cheng, C.L. Dennis, R.D. Shull, A.R.H. Walker, Influence of the colloidal environment on the magnetic behavior of cobalt nanoparticles, Langmuir 23 (2007) 11740–11746.
[9] T. Wen, W. Liang, K.M. Krishnan, Coupling of blocking and melting in cobalt ferrofluids, J. Appl. Phys. 107 (2010) 09B501.
[10] M.B. Morales, M.H. Phan, S. Pal, N.A. Frey, H. Srikanth, Particle blocking and carrier fluid freezing effects on the magnetic properties of Fe_3O_4-based ferrofluids, J. Appl. Phys. 105 (2009) 07B511.
[11] R. Di Corato, A. Espinosa, L. Lartigue, M. Tharaud, S. Chat, T. Pellegrino, C. Ménager, F. Gazeau, C. Wilhelm, Magnetic hyperthermia efficiency in the cellular environment for different nanoparticle designs, Biomaterials 35 (2014) 6400–6411.
[12] S. Sun, H. Zeng, Size-controlled synthesis of magnetite nanoparticles, J. Am. Chem. Soc. 124 (2002) 8204–8205.
[13] S. Sun, H. Zeng, D.B. Robinson, S. Raoux, P.M. Rice, S.X. Wang, G. Li, Monodisperse MFe_2O_4 (M=Fe, Co, Mn) nanoparticles, J. Am. Chem. Soc. 126 (2004) 273–279.
[14] B. Luigjes, S.M.C. Woudenberg, R. de Groot, J.D. Meeldijk, H.M. Torres Galvis, K. P. de Jong, A.P. Philipse, B.H. Erné, , Diverging geometric and magnetic size distributions of iron oxide nanocrystals, J. Phys. Chem. C 115 (2011) 14598–14605.
[15] D.R. Douslin, H.M. Huffman, Low-temperature thermal data on the five isomeric hexanes, J. Am. Chem. Soc. 68 (1946) 1704–1708.
[16] H.L. Finke, M.E. Gross, G. Waddington, H.M. Huffman, Low-temperature thermal data for the nine normal paraffin hydrocarbons from octane to hexadecane, J. Am. Chem. Soc. 76 (1954) 333–341.
[17] E.F. Westrum Jr., F. Grønvold, Magnetite (Fe_3O_4) heat capacity and thermodynamic properties from 5 to 350 K, low-temperature transition, J. Chem. Thermodyn. 1 (1969) 543–557.
[18] W.J. Atkinson, I.A. Brezovich, D.P. Chakraborty, Usable frequencies in hyperthermia with thermal seeds, IEEE Trans. Biomed. Eng. BME 31 (1984) 70–75.
[19] I. Andreu, E. Natividad, C. Ravagli, M. Castro, G. Baldi, Heating ability of cobalt ferrite nanoparticles showing dynamic and interaction effects, RSC Adv. 4 (2014) 28968–28977.
[20] R. Hergt, R. Hiergeist, M. Zeisberger, D. Schüler, U. Heyen, I. Hilger, W.A. Kaiser, Magnetic properties of bacterial magnetosomes as potential diagnostic and therapeutic tools, J. Magn. Magn. Mater. 293 (2005) 80–86.
[21] R.E. Rosensweig, Heating magnetic fluid with alternating magnetic field, J. Magn. Magn. Mater. 252 (2002) 370–374.
[22] J.-P. Fortin, F. Gazeau, C. Wilhelm, Intracellular heating of living cells through Néel relaxation of magnetic nanoparticles, Eur. Biophys. J. 37 (2008) 223–228.
[23] D.V. Berkov, N.L. Gorn, Susceptibility of the disordered system of fine magnetic particles: a Langevin-dynamics study, J. Phys: Condens. Matter 13 (2001) 9369–9381.
[24] J. Nowak, F. Wiekhorst, L. Trahms, S. Odenbach, The influence of hydrodynamic diameter and core composition on the magnetoviscous effect of biocompatible ferrofluids, J. Phys. Condens. Matter 26 (2014) 176004.